



Contents lists available at ScienceDirect

Journal of Rock Mechanics and Geotechnical Engineering

journal homepage: www.jrmge.cn

Full Length Article

Damage constitutive model of lunar soil simulant geopolymers under impact loading

Hanyan Wang^{a,b}, Qinyong Ma^{a,b,*}, Qianyun Wu^{a,b}

^a School of Civil Engineering and Architecture, Anhui University of Science and Technology, Huainan, 232001, China

^b Engineering Research Center of Underground Mine Construction, Ministry of Education, Anhui University of Science and Technology, Huainan, 232001, China

ARTICLE INFO

Article history:

Received 18 January 2023

Received in revised form

18 April 2023

Accepted 26 April 2023

Available online 14 November 2023

Keywords:

Lunar soil simulant geopolymer (LSSG)

Split Hopkinson pressure bar (SHPB) test

Constitutive model

Energy analysis

Failure mode

ABSTRACT

Lunar base construction is a crucial component of the lunar exploration program, and considering the dynamic characteristics of lunar soil is important for moon construction. Therefore, investigating the dynamic properties of lunar soil by establishing a constitutive relationship is critical for providing a theoretical basis for its damage evolution. In this paper, a split Hopkinson pressure bar (SHPB) device was used to perform three sets of impact tests under different pressures on a lunar soil simulant geopolymer (LSSG) with sodium silicate (Na_2SiO_3) contents of 1%, 3%, 5% and 7%. The dynamic stress–strain curves, failure modes, and energy variation rules of LSSG under different pressures were obtained. The equation was modified based on the ZWT viscoelastic constitutive model and was combined with the damage variable. The damage element obeys the Weibull distribution and the constitutive equation that can describe the mechanical properties of LSSG under dynamic loading was obtained. The results demonstrate that the dynamic compressive strength of LSSG has a marked strain-rate strengthening effect. Na_2SiO_3 has both strengthening and deterioration effects on the dynamic compressive strength of LSSG. As Na_2SiO_3 grows, the dynamic compressive strength of LSSG first increases and then decreases. At a fixed air pressure, 5% Na_2SiO_3 had the largest dynamic compressive strength, the largest incident energy, the smallest absorbed energy, and the lightest damage. The ZWT equation was modified according to the stress response properties of LSSG and the range of the SHPB strain rate to obtain the constitutive equation of the LSSG, and the model's correctness was confirmed.

© 2024 Institute of Rock and Soil Mechanics, Chinese Academy of Sciences. Production and hosting by Elsevier B.V. This is an open access article under the CC BY-NC-ND license (<http://creativecommons.org/licenses/by-nc-nd/4.0/>).

1. Introduction

With the boom in lunar exploration, an increasing number of countries are exploring lunar resources, which is a significant aspect of human society's development (Ouyang, 2004; Zheng et al., 2008a). Drilling and sampling, surface sampling, and sealing of the lunar surface for China's Chang'e–5 spacecraft were completed on 2 December 2020, and 1731 lunar samples were obtained (Xu et al., 2018; Qian et al., 2021; Zhang et al., 2022). Space sampling is a significant step in the study of lunar soil resources. The landing of spacecraft and drilling and sampling using a sampler during lunar exploration missions will have certain dynamic effects

on lunar soil (Prabu et al., 2022). The dynamic characteristics of lunar soil are crucial for future lunar base construction and should be considered in the design of lunar building load (Chayoomi et al., 2017; Liu et al., 2020).

Because the sizes of existing lunar soil samples are insufficient for engineering tests, developing a lunar soil simulant material for engineering research is an urgent matter. The JSC series lunar soil simulants developed by the Johnson Space Center of NASA are among the earliest to be developed and applied, and its raw material is volcanic ash (Ray et al., 2010; Song et al., 2019). The strength and deformation characteristics of JSC lunar soil simulants have been measured (Taylor et al., 2016; Wang et al., 2017). Japan's Shimizu Corporation's Space and Robotic Systems Division has developed two lunar simulations, i.e. MKS-1 and FMK-1, based on Apollo 14 lunar soil samples. They employ basalt as the raw material, and their main purpose is to meet the needs of in situ resource utilization research on the moon (Kanamori et al., 1998; Uesugi et al., 2009). The CAS-1 lunar soil simulant developed in China employs low-titanium basaltic scoria and has scientific

* Corresponding author. School of Civil Engineering and Architecture, Anhui University of Science and Technology, Huainan, 232001, China.

E-mail address: qymaah@126.com (Q. Ma).

Peer review under responsibility of Institute of Rock and Soil Mechanics, Chinese Academy of Sciences.

research significance for future moon programs (Zheng et al., 2008b). Table 1 lists the lunar soil simulants from various countries and their uses.

Lunar soil has a very low density, making it infeasible as a building or foundation material for moon construction and, thus, requires strengthening (Farries et al., 2021; Zhou et al., 2021). Alexiadis et al. (2017) used a lunar soil simulant as the raw material and NaOH as an alkali activator to prepare geopolymers with compressive strength up to 18 MPa. Geopolymers can effectively improve the strength of lunar soil simulants. At present, the literature has focused on the static mechanical properties of lunar soil simulant geopolymers (LSSGs). Montes et al. (2015) first attempted to prepare a geopolymer by using lunar soil simulant as raw material in 2015. They found that the materials with a larger specific surface area and higher content of silicon and aluminum elements were more likely to improve the strength of the geopolymer. Momi et al. (2021) studied the influences of urea and water on the mechanics and rheological properties of geopolymers in a lunar soil simulant under the action of a NaOH alkali initiator. Prabu et al. (2022) studied the dynamic characteristics of a lunar soil analog (LSS-ISAC-1) through a cyclic triaxial test and obtained its shear modulus, damping ratio, and Poisson's ratio. However, studies on the dynamic properties of LSSG remain scarce.

Accordingly, Na₂SiO₃ was used as an alkali activator in this study to prepare an LSSG. A split Hopkinson pressure bar (SHPB) test was performed as a uniaxial impact compression test. The effects of Na₂SiO₃ content, curing age and impact pressure on the dynamic compressive strength of LSSG were studied. The ZWT constitutive model was simplified by considering the dynamic characteristics of LSSG, and a rate-type damage constitutive equation was derived. Additionally, a viscoelastic constitutive model with nonlinear, Maxwell and damage bodies based on the Weibull distribution was proposed and experimentally verified.

Table 1
Development of lunar soil simulant in different countries.

Country	Lunar soil simulant	Research and development institution	Raw material	Application area
USA	GRC	NASA Green Research Center	Quartz sand	Research on engineering application
	MLS-1	The University of Minnesota	Basalt	Scientific engineering research
UK	SSC-1	Surrey Space Center	Quartz sand	Research on engineering application
	SSC-2		Garnet	
Japan	FJS-1	Space and Robotic Systems Department of Shimizu Corporation	Basaltic lava	Research on engineering application
	MKS-1			
Canada	OB-1	University of New Brunswick	Plagioclase	Research on engineering application
China	CAS-1	Chinese Academy of Sciences	Basalt	Scientific engineering research
	CLRS-1	Chinese Academy of Sciences and National Astronomical Observatories	Volcanic ash	
	CLRS-2		Volcanic ash	
	TJ-1	Tongji University	Volcanic ash	Research on engineering application
	CUG-1A	China University of Geosciences	Volcanic ash	
	LBD	North China Vehicle Research Institute	Volcanic ash, hematite sand	

2. Test materials and equipment

2.1. Test materials

The choice of crushed basalt as a lunar soil simulant material in this experiment was informed by similarities in the material composition between basalt and lunar soil (Qian et al., 2020; Ma and Wang, 2022), as shown in Fig. 1 (Schleppi et al., 2019; Zarzycki and Katzer, 2019; Engelschiön et al., 2020). The collected basalt was dried, crushed, screened and ground to make the lunar soil simulant (Fig. 2), and the obtained particle gradation is shown in Fig. 3. The grain size of the lunar soil simulant in the literature is shown in Fig. 4 (Jiang et al., 2012; Zou et al., 2016; Monkul and Dacic, 2017).

Dissolving sodium silicate in the water results in a colorless transparent viscous liquid with a pH value of 11–13 and a modulus of 1.2.

2.2. Design of the SHPB test

The effects of curing age (7 d and 28 d), Na₂SiO₃ amount (1%, 3%, 5% and 7 %), and air pressure (0.2 MPa, 0.3 MPa and 0.4 MPa) on the dynamic compressive properties of LSSG were analyzed. Table 2 lists the test schemes.

2.3. SHPB device

A SHPB device mainly includes power launching, pressure bar test, signal receiving and acquisition, and signal processing devices (Ma and Gao, 2018). Fig. 5 depicts a schematic diagram of the main device.

The striker, incident bar, and transmission bar used in the test were all made of steel. The diameter of the pressure bar was 50 mm, and its density was 7.8 g/cm³, whereas the elastic modulus of all bars was 210 GPa. The transmission velocity of the stress wave was 5190 m/s. The stress and strain of LSSG were obtained using strain gauges fixed on the incident and transmitted bars and the signal acquisition system. Because the wave impedance of LSSG is small, a sensitivity coefficient of 110% ± 5% was used in the semiconductor strain gauge fixed to the transmission bar, whereas that of the resistance strain gauge on the incident bar was 2% ± 5%.

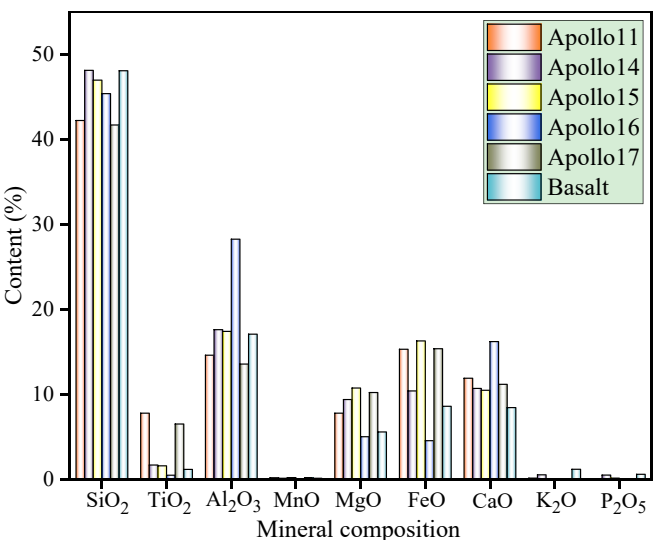


Fig. 1. Comparison of lunar soil mineral composition.



Fig. 2. Photograph of the lunar soil simulant.

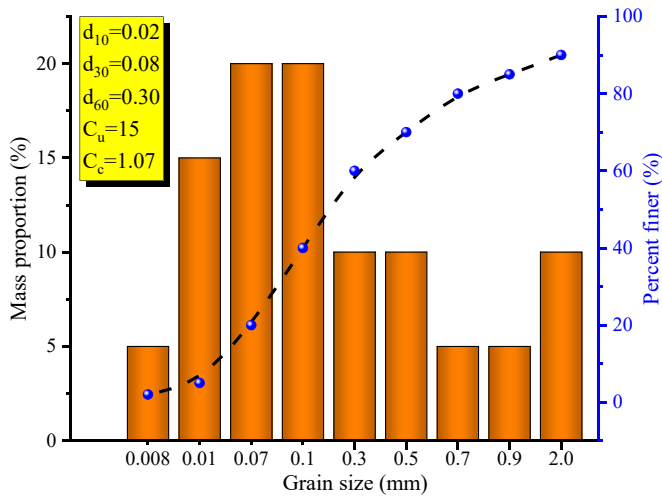


Fig. 3. Particle size distribution of the lunar soil simulant.

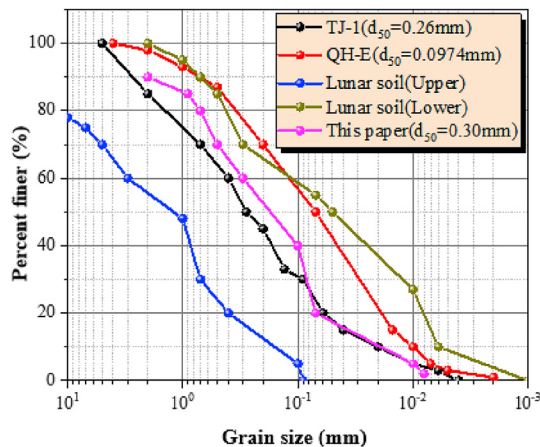


Fig. 4. Lunar soil grain sizes present in the literature.

SHPB is mainly used for testing the relationship between stress and strain in materials under one-dimensional (1D) stress and strain rates of $100\text{--}1000\text{ s}^{-1}$. To satisfy some test conditions, the following assumptions are made:

- (1) The transmission of a stress wave in the bar conforms to 1D stress wave theory.
- (2) The inertia effect of samples can be ignored.
- (3) The stress and strain in the samples are homogeneous.
- (4) The friction effect of the compression surface between the sample and bar can be ignored (Xue et al., 2021; Xiao et al., 2021).

The transmission mode of the stress wave in the bar is shown in Fig. 6.

2.4. Test data processing

To ensure stress uniformity during loading in the SHPB test, all bars and specimens were adjusted before the test to ensure collinearity in the pressure bar and sample. In addition, a waveform shaper was used to reduce waveform oscillation and ensure an appropriate rise time of the incident pulse, thus effectively ensuring constant strain rate loading (Xia et al., 2008). The original waveform was obtained by smoothing the wave collected on the oscilloscope and determining the baseline, as shown in Fig. 7. The stress, strain and strain rates in the samples were calculated using the three-wave-method formula from the original incident, reflected and transmitted waves collected (Song and Hu, 2005).

Balanced stress is necessary to ensure the stress uniformity at both ends of the samples and the test accuracy. The relationships of incident, reflected, transmitted, and incident + reflected stresses with time in the pressure bars at both ends of the sample were obtained, as shown in Fig. 8.

As shown in Fig. 8, the waveforms of the transmitted wave and incident + reflected wave are very similar, which suggests that the LSSG sample reached stress equilibrium during the impact process.

Due to the large dispersion during preparation of LSSG samples, four groups of parallel samples were created in the experiment for each group of variables, the dispersion of the LSSG wave velocity was analyzed, and the coefficient of variation was determined to avoid the influence of LSSG defects and ensure the test accuracy. Notably, a larger coefficient of variation results in a greater dispersion. To meet the experimental requirements specified in GB/T23561.1-2009 (2009), a coefficient of variation less than 20% was used, as listed in Table 3.

3. Analysis of dynamic compression performance of LSSG

3.1. Dynamic stress–strain curve

3.1.1. Change in stress–strain curve of LSSG with curing age

Fig. 9 shows the dynamic stress–strain curves of LSSG at a strain rate of 57.435 s^{-1} and curing ages of 7 d and 28 d (Ma et al., 2019). As shown in Fig. 9a, the linear elastic stage in the stress–strain curve is longer at the curing age of 7 d. When 1% Na_2SiO_3 was used, a prepeak elasto-plastic plateau stage was observed in the stress–strain curve. When the Na_2SiO_3 content was increased from 3% to 7%, the peak stress in the curve first increased and then decreased. The maximum peak stress was achieved by using 5% Na_2SiO_3 . Compared with samples containing 1% Na_2SiO_3 , the peak strain in the samples containing 5% Na_2SiO_3 increased significantly, indicating that the LSSG ductility could be effectively improved by adding Na_2SiO_3 at the early stage (Koohestani et al., 2021).

Fig. 9b shows the stress–strain curve of LSSG with a curing age of 28 d. When 1% Na_2SiO_3 was added, the stress–strain curve exhibited prominent brittle failure characteristics; specifically, before peak strength was reached, the stress increased with strain, and after peak stress was reached, the stress decreased to the residual stress with an increase in strain, at which point the sample

Table 2
Design of the SHPB test with different air pressures.

Curing age (d)	Na ₂ SiO ₃ content (%)	Sample number		
		0.2 MPa	0.3 MPa	0.4 MPa
7	1	N-1-0.2-7	N-1-0.3-7	N-1-0.4-7
	3	N-3-0.2-7	N-3-0.3-7	N-3-0.4-7
	5	N-5-0.2-7	N-5-0.3-7	N-5-0.4-7
	7	N-7-0.2-7	N-7-0.3-7	N-7-0.4-7
28	1	N-1-0.2-28	N-1-0.3-28	N-1-0.4-28
	3	N-3-0.2-28	N-3-0.3-28	N-3-0.4-28
	5	N-5-0.2-28	N-5-0.3-28	N-5-0.4-28
	7	N-7-0.2-28	N-7-0.3-28	N-7-0.4-28

Note: N-x-y-z: x represents the x parallel sample, y represents the air pressure, and z represents the curing days of the sample.

failed. When Na₂SiO₃ content was increased from 3% to 7%, the stress–strain curve became steeper and “narrow,” whereas the curve shifted leftward compared to that at a curing age of 7 d. This indicates that with an increase in curing age, the ductility of LSSG decreased, and the brittle failure became more marked (Xiao et al., 2022).

3.1.2. Change in dynamic stress–strain curve of LSSG with strain rate

Fig. 10 shows the changes in the dynamic compressive stress–strain curves of LSSG with strain rate. The following findings can be inferred:

- (1) The impact dynamic peak stress of LSSG has a prominent effect on the strain rate, i.e. with increasing strain rate, the peak strength continuously increases, especially when 1% Na₂SiO₃ is used, and the change in peak stress value is more prominent.
- (2) Under different strain rates, the dynamic stress–strain curves exhibited the same general trend, which could be divided into pore closure, elastic, plastic yield, and the failure states.
- (3) When the strain rate increased, the strain corresponding to the peak stress of the sample also increased, which may be attributable to the pressure increase caused by the gap inside the LSSG being unable to expand and extend over the short duration. On the other hand, the number of cracks in other areas increased, resulting in the increase in peak strain.
- (4) When 5% Na₂SiO₃ was added, the curve exhibited almost linear growth before the peak stress was reached. Moreover,

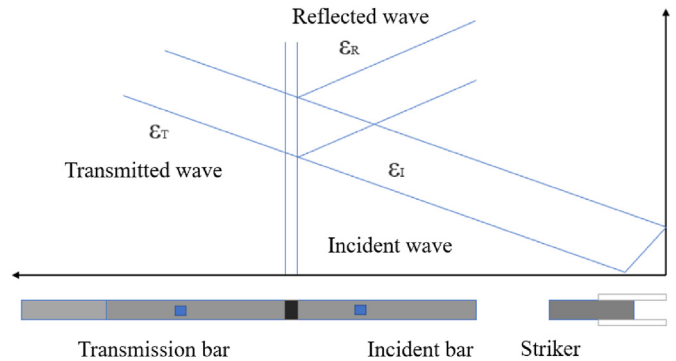


Fig. 6. Stress wave transmission in SHPB.

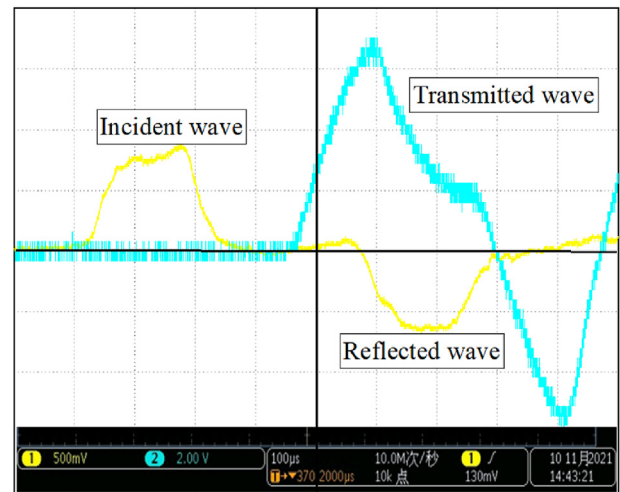


Fig. 7. Original waveform of LSSG.

the curve exhibited a cliff drop at the final failure stage, indicating that the LSSG with 5% Na₂SiO₃ has good linearly elastic characteristics.

3.1.3. Typical stress–strain curve of LSSG

As shown in Fig. 11, the dynamic stress–strain curves of LSSG exhibited similar characteristics under different curing ages and

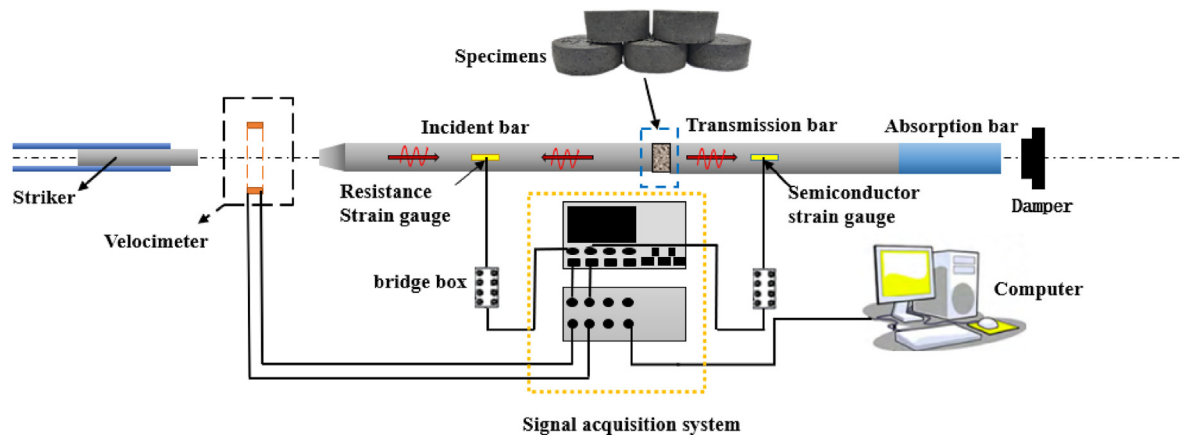


Fig. 5. Schematic diagram of the SHPB test device.

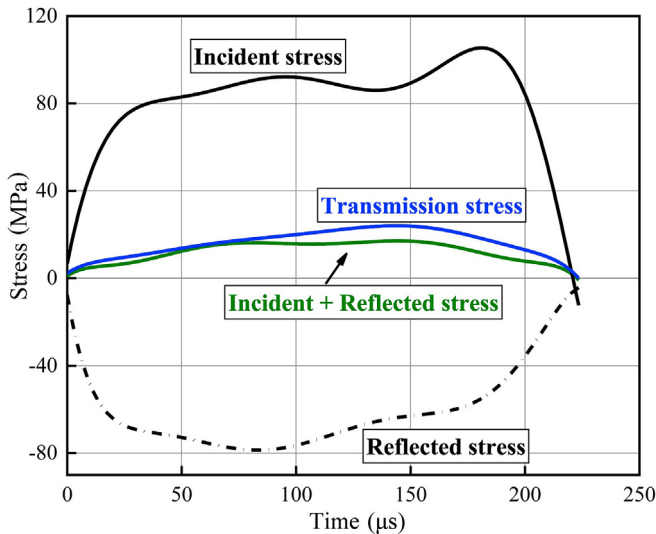


Fig. 8. Verification of stress uniformity.

strain rates across the following stages (Gao et al., 2022; Liu and Li, 2022):

- (1) Grain compaction state (OA): Under impact loads, the dynamic stress–strain curve rises rapidly. The impact load results in closely spaced microcracks and improves the compressive and deformation resistance of the LSSG.
- (2) Elastic state (AB): Stress and strain increase proportionately. Moreover, the stress wave in the sample reaches stress balance after several reflections. Meanwhile, the external impact load cannot create new cracks in the sample, the sample remains elastic, and the slope of the stress–strain curve remains constant. The slope at this stage is taken as the dynamic elastic modulus of the LSSG.
- (3) Crack-appearance state (BC): The slope of the stress–strain curve is smaller, and the stress increases slowly with the increase in strain, changing the state of the specimen from elastic to plastic.
- (4) Crack continued propagation state (CD): During this stage, the dynamic stress continues to increase, but the slope of the curve approaches zero. As the load continues to increase, the cracks in the sample expand, and the sample can still bear some load before the peak stress.
- (5) Failure state (DE): After the sample reaches the peak stress, the slope of the stress–strain curve becomes negative, and the stress decreases at different rates under different air pressures. Meanwhile, the sample has fully lost its bearing capacity, and severe deformation and failure occur.

3.2. Dynamic compressive strength

The variation law of the dynamic strength of LSSG under different curing ages and Na_2SiO_3 contents is shown in Fig. 12. The following rules can be inferred:

- (1) After adding Na_2SiO_3 , the dynamic compressive strength of LSSG markedly improves. Their strengths under different curing ages exhibit the same law when the Na_2SiO_3 content increases. It increases slowly and then decreases, and the maximum strength is reached when 5% Na_2SiO_3 is used.

- (2) With increasing curing age, the dynamic strength continuously increases. When the strain rate is 57.435 s^{-1} , the 28 d dynamic compressive strength of the sample with 1% Na_2SiO_3 is approximately twice as high as that of the 7 d strength. With the increase in Na_2SiO_3 from 3% to 7%, the 28 d dynamic strength of samples increases by 24.53%, 13.11% and 13.9% compared with that of the sample with 7 d of curing.
- (3) When the strain rate is 82.516 s^{-1} and the Na_2SiO_3 content increases from 1% to 7%, the 28 d dynamic strength increases by 62.51%, 30.4%, 20.96% and 29.7%, compared with the 7 d dynamic strength. When the strain rate is 109.825 s^{-1} , with the increase in Na_2SiO_3 content from 1% to 7%, the 28 d dynamic strength of LSSG increases by 78.52%, 28.7%, 36% and 37.56% compared with the 7 d dynamic strength.

3.3. Variation in dynamic strength with strain rate

To study the change in the LSSG dynamic compressive strength with strain rate, the compressive strength and strain rates of samples with Na_2SiO_3 contents of 1%, 3%, 5% and 7% were analyzed, as shown in Fig. 13. The following rules can be derived:

- (1) The strain rates of all samples are in the range of $40\text{--}110 \text{ s}^{-1}$. With the increase in strain rate, the dynamic compressive strength of LSSG tends to increase.
- (2) The slopes of the fitted curves of the dynamic compressive strength and the average strain rate corresponding to Na_2SiO_3 contents of 1%, 3% and 5% are approximately the same.
- (3) When the strain rate increases from 50 s^{-1} to 100 s^{-1} , the variation range of dynamic compressive strength of LSSG with 7% Na_2SiO_3 is the largest, indicating that the dynamic compressive strength of LSSG with a higher Na_2SiO_3 content is more strongly affected by the average strain rate.

4. Failure patterns of LSSG

The mechanism by which Na_2SiO_3 improves the lunar soil simulant is by closely joining the particles inside the sample through Na_2SiO_3 cementation. Inevitably, pores and microcracks will form in the internal structure. These defects also deteriorate the mechanical properties. During dynamic tests, the microcracks in the LSSG expanded under increasing impact loads, and the outer part of the samples exhibited macroscopic cracks (Li et al., 2021). The dynamic failure patterns of LSSG are shown in Fig. 14.

Fig. 14 shows that the Na_2SiO_3 content greatly influences LSSG failure. The main influence rules are described as follows (Han et al., 2022; Song et al., 2022a):

- (1) When 1% Na_2SiO_3 was added and the strain rate was 54.069 s^{-1} , the sample was broken. Moreover, the breakage was greater at a strain rate of 62.82 s^{-1} . With the strain rate increasing up to 87.105 s^{-1} , the LSSG sample was crushed, with almost no large fragments remaining. Therefore, with an increase in pressure, the stress wave does not rapidly pass through the existing crack area in the sample. It directly followed the shortest path through the particle, resulting in a relatively large degree of crushing.
- (2) When the Na_2SiO_3 content was 3%, the sample breakage became apparent at a strain rate of 54.297 s^{-1} ; however, this was observed in only a small portion of the samples. With

Table 3
Experimental parameters of the lunar soil simulant.

Air pressure (MPa)	Na ₂ SiO ₃ (%)	Strain rate (s ⁻¹)	Wave velocity (m/s)	Coefficient of variation (%)
0.2	1	54.069	1320.24	4.2
	3	54.297	1890.58	3.93
	5	57.435	2004.11	5.66
	7	57.953	1500.36	4.13
0.3	1	62.82	1340.57	5.1
	3	78.12	1875.14	3.33
	5	82.516	1946.68	2.21
	7	84.715	1420.32	2.09
0.4	1	87.105	1229.44	6.79
	3	90.426	2180.5	4.01
	5	109.825	1967.71	2.27
	7	97.651	1433.83	3.24

the strain rate increasing from 78.12 s⁻¹ to 90.426 s⁻¹, increasingly larger parts of the sample were broken. However, compared with the 1% Na₂SiO₃ samples, the part of the test block that was broken was larger than that which was crushed.

- (3) The samples with 5% Na₂SiO₃, unlike those with 1% and 3% Na₂SiO₃, maintained integrity under a strain rate of 57.435 s⁻¹. However, only some slight cracking appeared, and the residual strength was relatively large at this time. When the strain rate was 82.516 s⁻¹, large cracks appeared on the LSSG failure surface, and the sample was divided into two parts, which was accompanied by the appearance of small cracks. With the continuous increase in strain rate, more pronounced failure characteristics were observed. LSSG was divided into three parts by additional cracks, and the final failure was crushing along the axial pressure direction (Xue et al., 2021).
- (4) For the samples with 7% Na₂SiO₃, when the strain rate was 57.953 s⁻¹, the failure characteristics observed were minor, with cracks only appearing at the edge of the failure surface without extending further. When the strain rate increased to 97.651 s⁻¹, the cracks appeared on the surface of large fragments. Notably, axial splitting failure was observed.

5. Energy dissipation in SHPB test

5.1. Principle and calculation of energy dissipation

The destruction of the LSSG samples is accompanied by energy dissipation. Moreover, energy conversion is irreversible and results in deformation. The study of energy conversion in LSSG under impact load is beneficial for elucidating the failure mechanism of the samples (Zheng et al., 2021).

According to the energy conversion principle and stress wave transfer rule, the incident energy Q_I , reflected energy Q_R , and transmitted energy Q_T can be calculated as follows:

$$\left. \begin{aligned} Q_I(t) &= E_0 C_0 A_0 \int_0^t \varepsilon_I^2(t) dt \\ Q_R(t) &= E_0 C_0 A_0 \int_0^t \varepsilon_R^2(t) dt \\ Q_T(t) &= E_0 C_0 A_0 \int_0^t \varepsilon_T^2(t) dt \end{aligned} \right\} \quad (1)$$

The absorbed energy of the sample when failure occurs is written as follows:

$$Q_S(t) = Q_I(t) - Q_R(t) - Q_T(t) \quad (2)$$

In general, the energy absorbed by LSSG is transformed into breaking energy. When the dissipative energy in the sample decreases, the cracks appear, the sample deforms less, and the incidence of failure decreases.

5.2. Energy law in SHPB test

Fig. 15 shows the energy changes in LSSG containing 5% Na₂SiO₃ under different strain rates. The incident and absorbed energy in LSSG increases continuously with time, but the increment differs. When the increase rate is slow, it stabilizes after a certain duration.

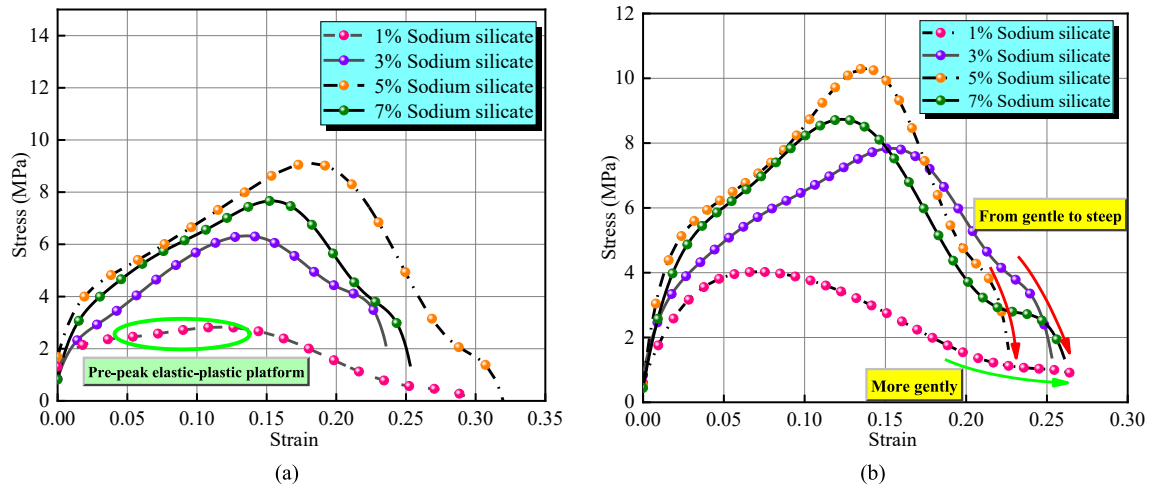


Fig. 9. Dynamic stress–strain curves of LSSG at different curing ages: (a) 7 d, and (b) 28 d.

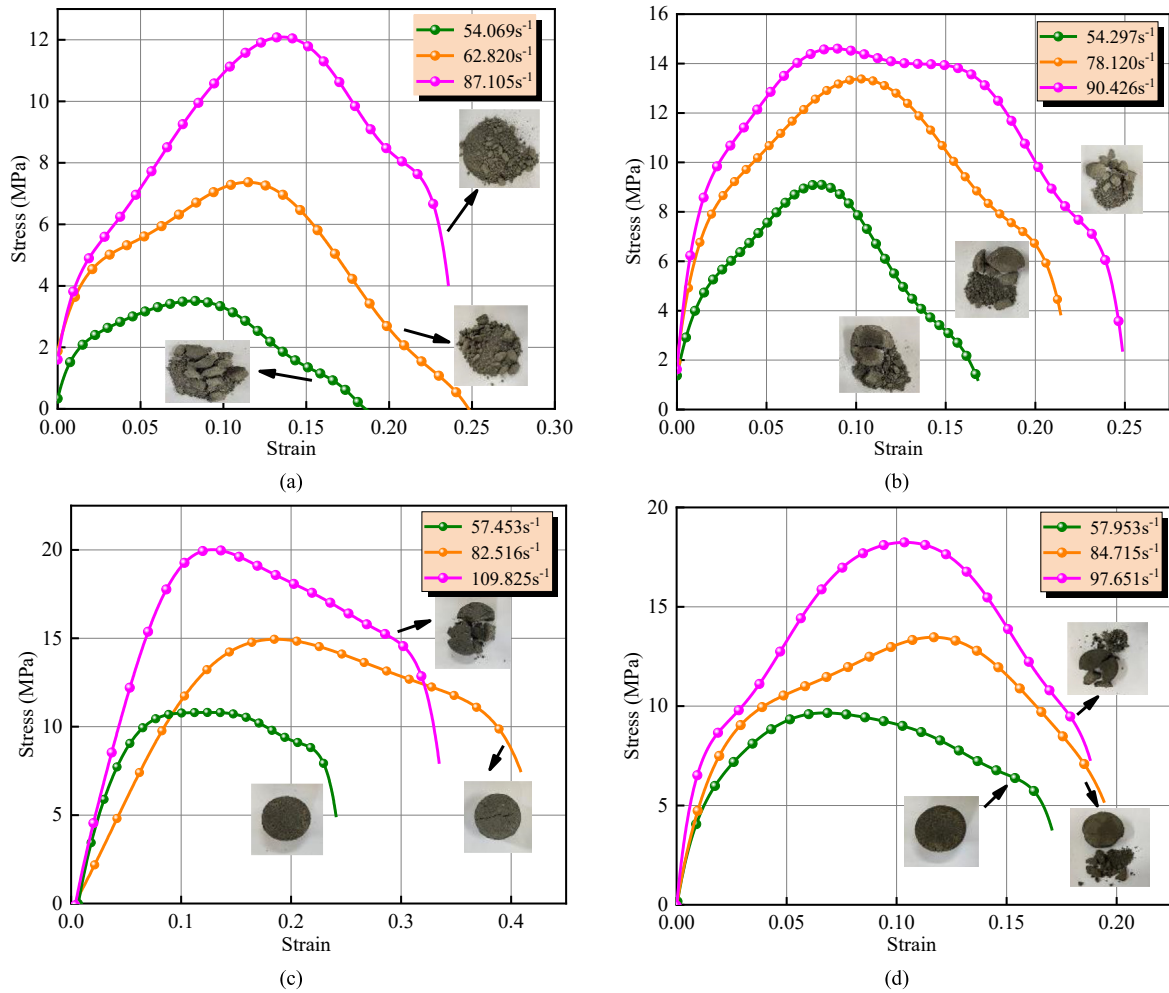


Fig. 10. LSSG stress–strain curves under different strain rates: (a) 1% Na_2SiO_3 , (b) 3% Na_2SiO_3 , (c) 5% Na_2SiO_3 , and (d) 7% Na_2SiO_3 .

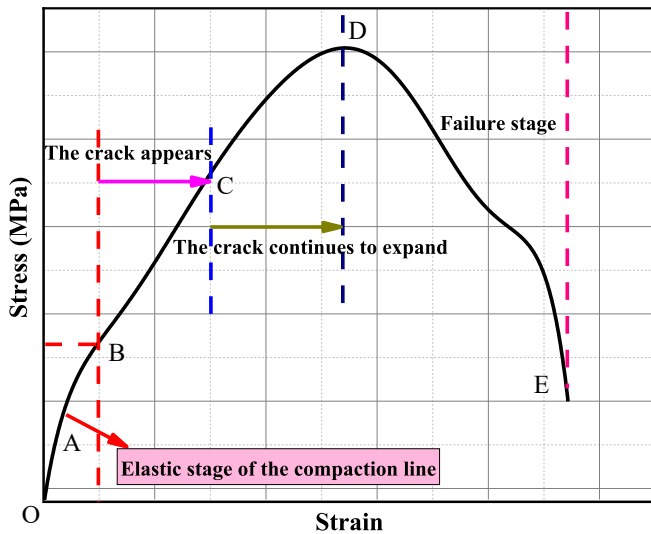


Fig. 11. Typical dynamic stress–strain plot of LSSG.

Regarding the incident energy of the sample, however, the change trend is not prominent with the increase in time (Ma et al., 2018). Compared with the incident energy, the value of the absorbed

energy was very small. At the strain rates of 57.435 s^{-1} , 82.516 s^{-1} and 109.825 s^{-1} , the magnitudes of the incident energy were approximately 9, 22 and 16 times that of the absorbed energy.

Fig. 16 shows the influence curve of different Na_2SiO_3 contents (1%, 3%, 5% and 7%) on the energy variation of LSSG. Noticeably, under the same pressure, LSSG with 5% Na_2SiO_3 had the highest and lowest incident and absorbed energy, respectively. The absorbed energy in the sample with a Na_2SiO_3 content of 1% was significantly higher than that of other samples. The peak values were 1.47, 4.5 and 1.92 times the absorbed energy of the samples with Na_2SiO_3 contents of 3%, 5% and 7%, respectively.

The aforementioned observation is attributable to a lower Na_2SiO_3 content, resulting in a worse bonding performance between the particles in the sample and the appearance of more cracks. Under axial air pressure, the energy absorbed by the LSSG was manifested in the expansion of external cracks, resulting in the samples entering an unstable state (Fu et al., 2017; Li et al., 2019).

It is important to determine the magnitude of energy absorbed by LSSG under different strain rates. Accordingly, the absorbed energy of LSSG was calculated. Fig. 17 presents the relationship among absorbed energy, sodium silicate content and strain rate, which could be written as follows:

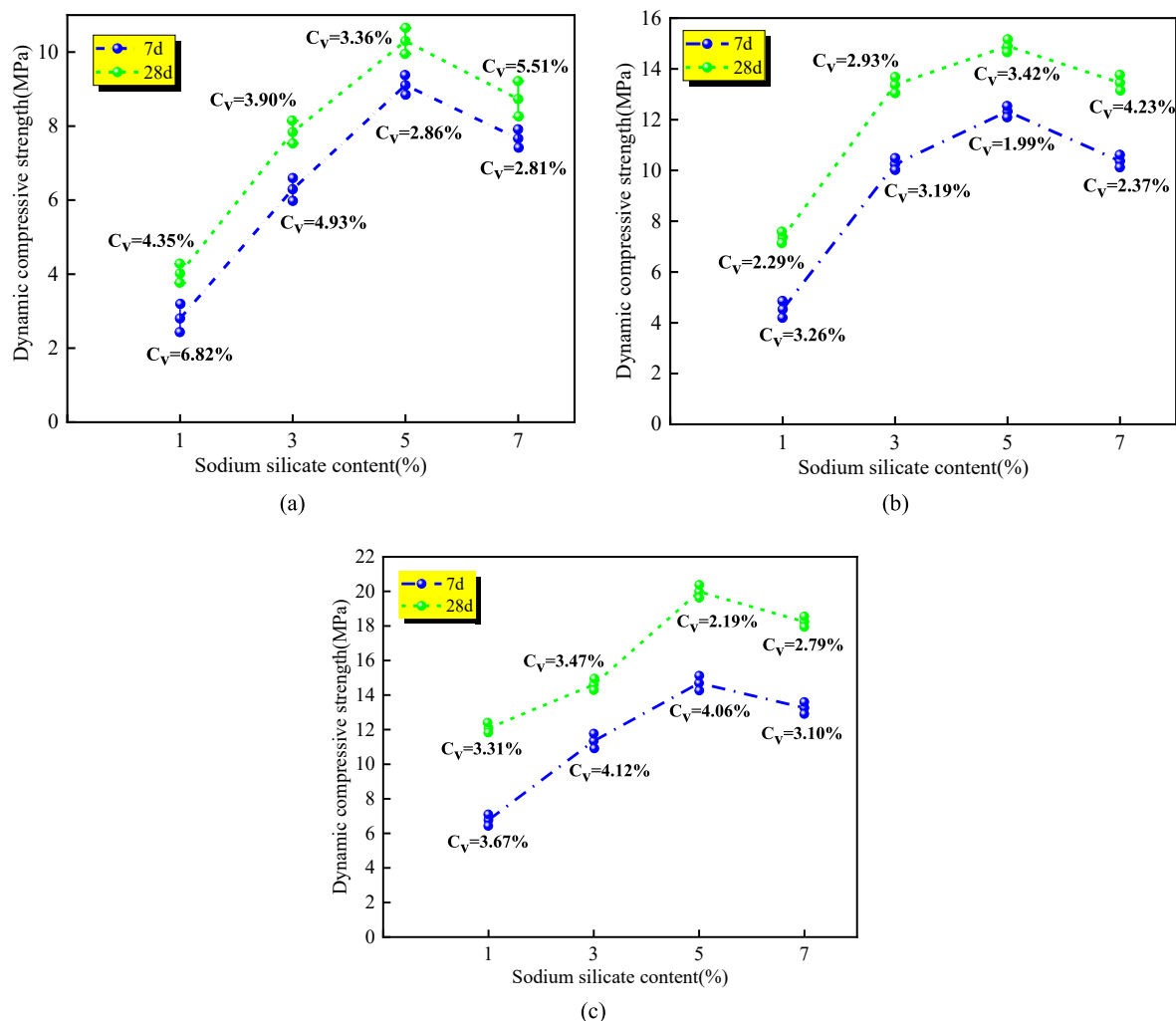


Fig. 12. Dynamic strength of LSSG under different Na_2SiO_3 contents: (a) 57.435 s^{-1} , (b) 82.516 s^{-1} , and (c) 109.825 s^{-1} .

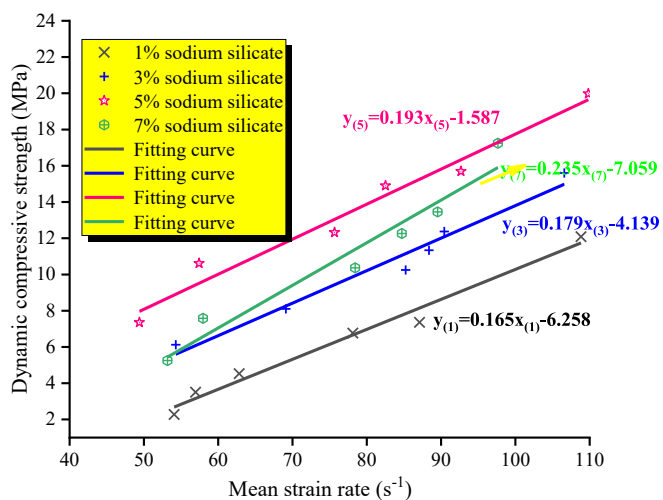


Fig. 13. Relationship between dynamic compressive strength and strain rate.

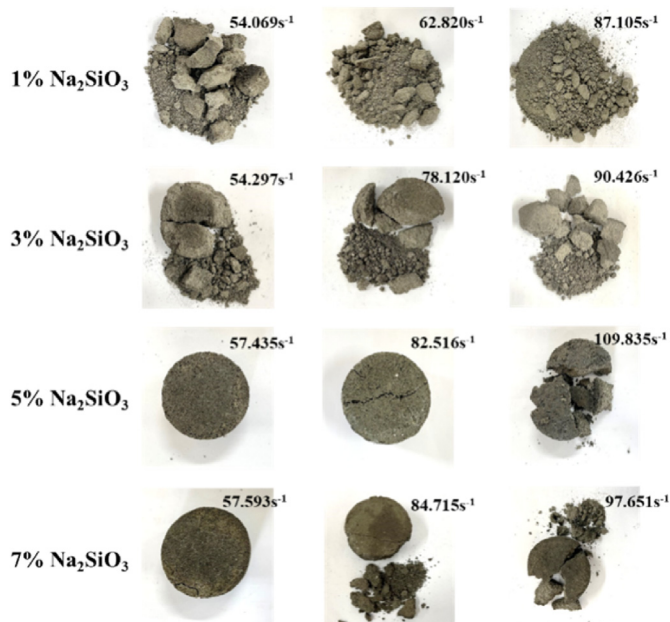


Fig. 14. Failure modes of specimens in dynamic tests.

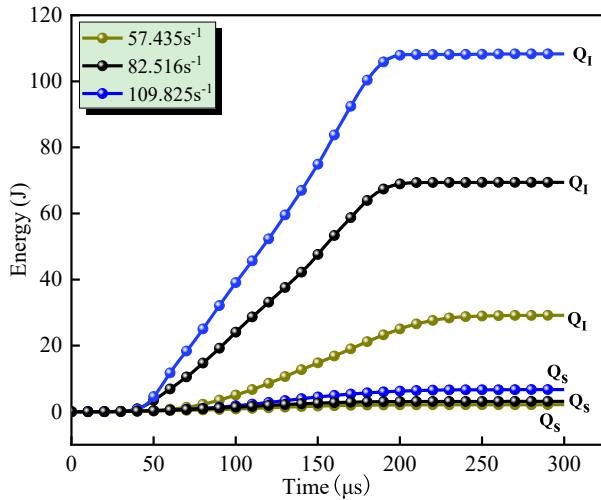


Fig. 15. Energy variation curves of LSSG under different air pressures.

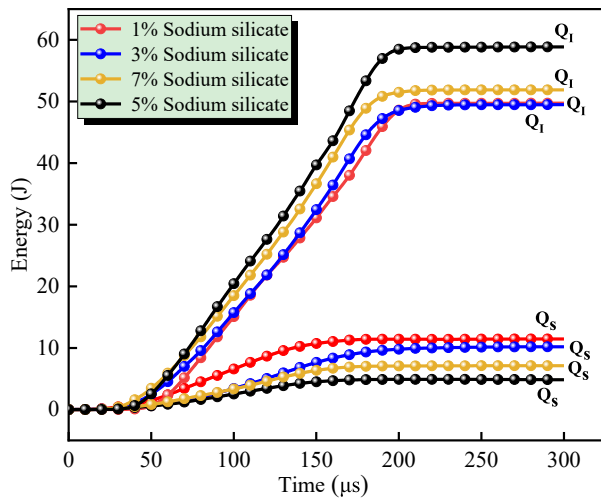


Fig. 16. Energy variation curves of LSSG with Na₂SiO₃ content.

$$Q_s = -15.436 - 3.0091N + 0.65\dot{\epsilon} + 0.355N^2 - 0.0027\dot{\epsilon}^2 - 0.0149N\dot{\epsilon} \quad (3)$$

where Q_s represents the absorbed energy (J), ϵ represents the strain, and N represents the Na₂SiO₃ content (%).

Fig. 18 depicts the relationship of absorbed energy with air pressure. The absorbed energy (Q_s) and air pressure (P) have a strong linear relation. The fitting equations are listed in Table 4.

Fig. 18 shows that the absorbed energy of LSSG increases as air pressure increases, and the absorbed energy increases by approximately 1.18, 1.21, 1.94 and 0.78 times, respectively, when the air pressure increases from 0.2 MPa to 0.4 MPa. This indicates that with the continuous increase in air pressure, the energy absorption ability of the sample is strengthened, as manifested by an increasing number of cracks in the sample. Among them, the absorbed energy of LSSG with 5% Na₂SiO₃ increases, and the sample is less damaged than other samples.

The Samples containing 5% Na₂SiO₃ were analyzed to determine the link between failure mode, absorbed energy per unit volume, and strain rate, and their relationships are shown in Fig. 19.

As shown in Fig. 19, the absorbed energy per unit volume in LSSG increases with the average strain rate, which indicates the presence of a certain correlation between the absorbed energy of the LSSGs and the average strain rate. When the average strain rate increases, the number of cracks in the sample continuously increases, which results in the increasing absorbed energy per unit volume. Meanwhile, the failure mode of the samples gradually changes from minor failure to partial crushing with increasing strain rate (Song et al., 2022b; Xu et al., 2022).

Therefore, the absorbed energy per unit volume of LSSG can better reflect the failure mode and dynamic strength, and studying the absorbed energy of LSSG is helpful to make full use of its dynamic characteristics.

6. Dynamic damage constitutive model of LSSG

The ZWT model is generally used to describe the mechanical properties of materials. Specifically, it is suitable for elucidating the mechanical properties of geopolymer materials when the strain rate ranges from 10^{-4} s^{-1} to 10^3 s^{-1} . The constitutive model (Fig. 20) generally consists of a nonlinear elastic model, low-frequency Maxwell element, and high-frequency Maxwell element (Can et al., 2015).

The φ_1 and φ_2 ranges are $10-100 \text{ s}$ and $10^{-4}-10^{-6} \text{ s}$, respectively. Generally, φ_1 mainly controls the low strain rate part, whereas φ_2 controls the high strain rate part (Dong et al., 2018).

The ZWT model is described as follows:

$$\sigma = E_0\epsilon + \alpha\epsilon^2 + \beta\epsilon^3 + E_1 \int_0^t \dot{\epsilon} e^{-\frac{t-\delta}{\varphi_1}} d\delta + E_2 \int_0^t \dot{\epsilon} e^{-\frac{t-\delta}{\varphi_2}} d\delta \quad (4)$$

where σ is the dynamic stress; E_0 , α and β are the nonlinear elastic constants of the body; E_1 and E_2 are the elastic moduli of the Maxwell bodies; φ_1 and φ_2 are the low-frequency and high-frequency relaxation times, respectively; and δ is the time, whose value range is $[0, t]$.

Because the time scale of the SHPB test is very short (usually $1-100 \text{ μs}$), the low-frequency Maxwell body does not have enough time to relax. Therefore, it can be regarded as a linear elastic body with an elastic modulus of E_1 . Eq. (4) can be rewritten as

$$\sigma = E_0\epsilon + \alpha\epsilon^2 + \beta\epsilon^3 + E_1\epsilon + E_2 \int_0^t \dot{\epsilon} e^{-\frac{t-\delta}{\varphi_2}} d\delta \quad (5)$$

Because the first term in Eq. (5) is unrelated to the strain rate, it only represents the equilibrium mechanical effect of samples under impact loads. Moreover, LSSG exhibited the characteristics of small strain during the test, and $\alpha\epsilon^2 + \beta\epsilon^3$ is almost negligible (Xie and Yan, 2019). Thus, Eq. (5) can be rewritten as

$$\sigma = E^\Delta\epsilon + E_2 \int_0^t \dot{\epsilon} e^{-\frac{t-\delta}{\varphi_2}} d\delta \quad (6)$$

$$E^\Delta = E_0 + E_1 \quad (7)$$

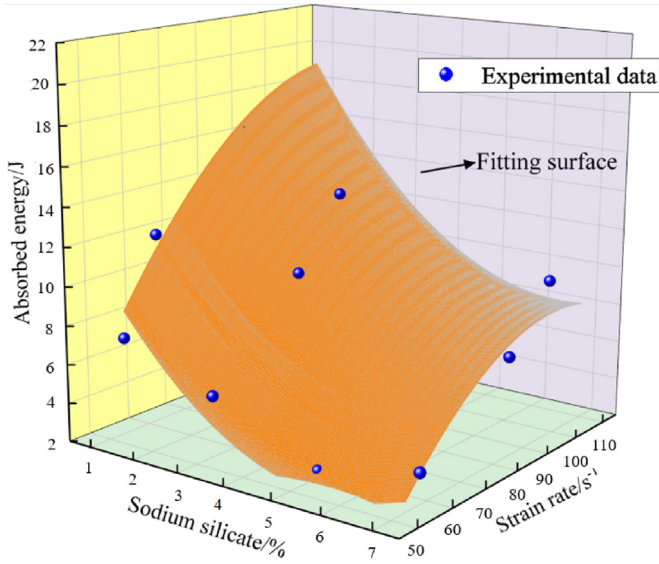


Fig. 17. Fitting surface among absorbed energy, sodium silicate content and strain rate of LSSG.

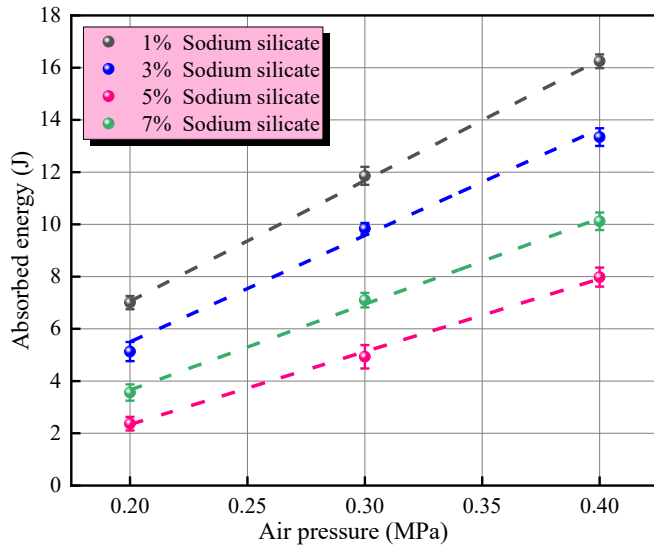


Fig. 18. Relationships between absorbed energy and air pressure of LSSG.

Table 4

Fitting equations ($Q_5 = aP + b$) for describing the relationships between absorbed energy and air pressure.

Na ₂ SiO ₃ content (%)	<i>a</i>	<i>b</i>	Correlation coefficient
1	46.23 ± 1.08	−2.19 ± 0.33	0.998
3	40.78 ± 4.52	−2.65 ± 1.4	0.975
5	27.89 ± 1.08	−3.24 ± 0.31	0.997
7	32.85 ± 1.66	−2.91 ± 0.51	0.994

Because the LSSG is a heterogeneous material with numerous internal cracks and holes, it undergoes deformation-induced damage when subjected to impact loads. Therefore, factors such as damage and deformation need to be considered in the constitutive model. The ZWT model is improved, and the continuous damage mechanics model is introduced to obtain the following equation:

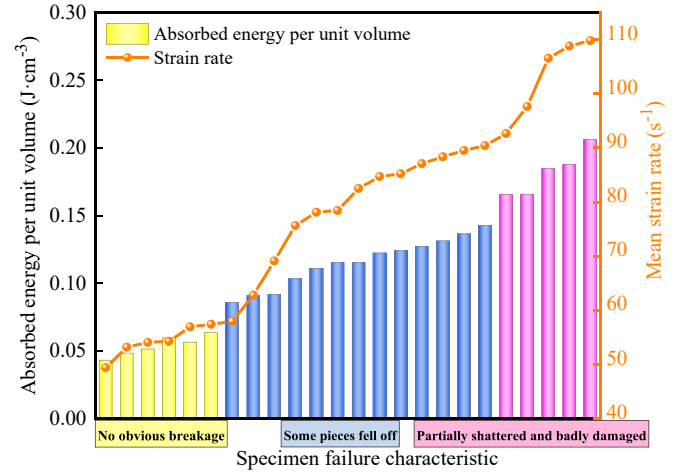


Fig. 19. Absorbed energy per unit volume and failure mode of LSSG.

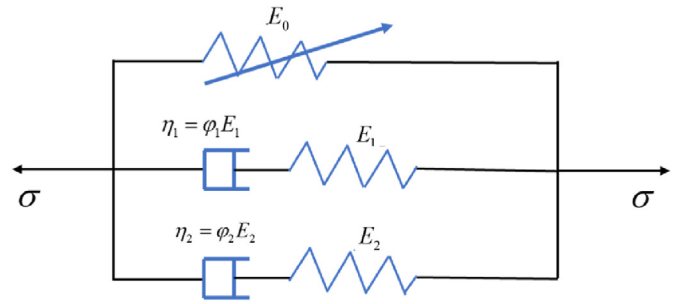


Fig. 20. ZWT model.

$$\sigma^* = (1 - D)\sigma \quad (8)$$

where σ^* is the effective stress. According to the literature (Wang et al., 2008; Zhou et al., 2022), all microelements in an LSSG obey the Weibull distribution, thus the damage factor of LSSG can be defined as follows:

$$D = \begin{cases} 0 & (\varepsilon \leq \varepsilon_1) \\ 1 - e^{-\frac{(\varepsilon - \varepsilon_1)^\omega}{\zeta}} & (\varepsilon > \varepsilon_1) \end{cases} \quad (9)$$

where ε_1 is the cumulative damage threshold strain of the LSSG, and $\varepsilon_1 = 0.5\varepsilon_{\max}$, in which ε_{\max} is the strain corresponding to the peak stress; and ω and ζ are the damage evolution parameters.

Therefore, the dynamic model of LSSG considering the damage can be obtained as follows (Ren et al., 2018), as shown in Fig. 21:

$$\sigma^* = \begin{cases} E^* \varepsilon + E_2 \varphi_2 \dot{\varepsilon} (1 - e^{-\frac{\varepsilon}{\varphi_2 \dot{\varepsilon}}}) & (\varepsilon \leq \varepsilon_1) \\ e^{-\frac{(\varepsilon - \varepsilon_1)^\omega}{\zeta}} [E^* \varepsilon + E_2 \varphi_2 \dot{\varepsilon} (1 - e^{-\frac{\varepsilon}{\varphi_2 \dot{\varepsilon}}})] & (\varepsilon > \varepsilon_1) \end{cases} \quad (10)$$

The equation fitting diagrams of LSSG with Na₂SiO₃ contents of 1%, 3%, 5% and 7% are drawn according to the constitutive model equation, and the correlation coefficients are all greater than 0.9, as shown in Fig. 22. The fitting results demonstrate that the experimental and theoretical curves are largely consistent, indicating that the constitutive model of the LSSG constructed in this paper

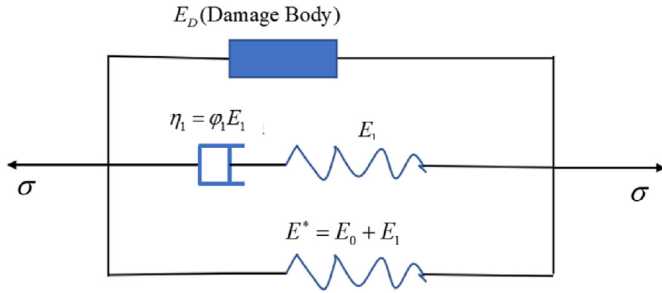


Fig. 21. Constitutive model of LSSG considering damage.

considering damage can better reflect its dynamic stress–strain characteristics.

7. Conclusions

The dynamic properties of LSSG are studied through an SHPB uniaxial impact test. The characteristics of the dynamic stress–strain curve are analyzed, and the dynamic compressive strength varies with the Na_2SiO_3 content, curing age and strain rate.

Moreover, the failure mode of LSSG is determined, and a damage constitutive model for LSSG is constructed. The following conclusions are drawn:

- (1) The dynamic stress–strain curve of LSSG mainly comprises the following five states: the particle compaction, linear elastic, crack appearance, crack extension, and failure states. The peak stress increases with the increasing strain rate. Under a strain rate of 109.825 s^{-1} , the peak stress can reach 20.03 MPa.
- (2) The dynamic compressive strength of LSSG with a curing age of 28 d is significantly higher than that of LSSG with a curing age of 7 d. The dynamic compressive strength of LSSG first increases and then decreases with increasing Na_2SiO_3 content, and the compressive strength is the largest when 5% Na_2SiO_3 is added.
- (3) The strain rates of all LSSGs ranges between 40 s^{-1} and 110 s^{-1} . With an increasing average strain rate, the dynamic compressive strength of LSSG exhibits an upward trend. The higher the Na_2SiO_3 content, the greater the influence of the average strain rate on the dynamic compressive strength.
- (4) The failure characteristics of LSSG under different strain rates differ under impact loading. The higher the strain rate, the

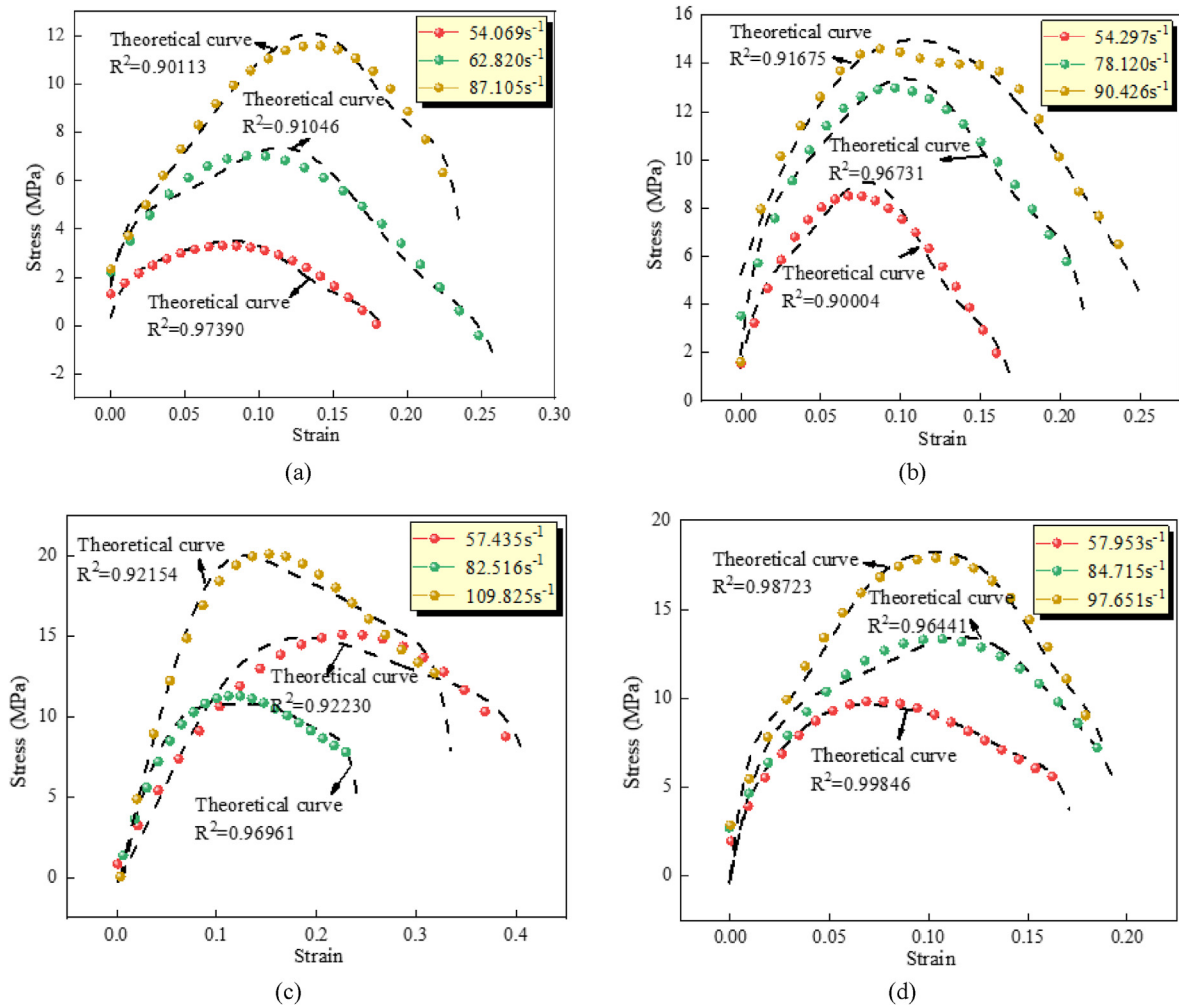


Fig. 22. Verification of the LSSG constitutive equation considering damage: (a) 1% Na_2SiO_3 , (b) 3% Na_2SiO_3 , (c) 5% Na_2SiO_3 , (d) 7% Na_2SiO_3 .

more severe the specimen fracture. When the LSSG with 1% Na_2SiO_3 is damaged, the sample is in a crushed state, with almost no large fragments. With the continuous increase in Na_2SiO_3 , the damage degree of the sample decreases markedly. When the Na_2SiO_3 content is 5%, no crushing is accompanied with damage to the sample. Only the number of cracks increases, and the ultimate failure is through crushing along the axial pressure direction.

- (5) A change in energy during impact loading occurs in the impact test on the LSSG. Under the same pressure, the incident energy of LSSG with a Na_2SiO_3 content of 5% is the largest, and the absorbed energy is the smallest; the absorbed energy of the sample with a Na_2SiO_3 content of 1% is the highest. This indicates that the damage to the sample is the severest at this dosage.
- (6) The ZWT equation is simplified based on the analysis of the ZWT model and the linear stress–strain curve obtained from the SHPB impact test. Moreover, the dynamic constitutive model of LSSG is established by comparing the stress–strain curves for different strain rates. The results demonstrate that the constitutive model is in a good agreement with the constitutive curve of LSSG obtained from the test.

Declaration of competing interest

The authors declare that they have no known competing financial interests or personal relationships that could have appeared to influence the work reported in this paper.

References

- Alexiadis, A., Alberini, F., Meyer, M.E., 2017. Geopolymers from lunar and martian soil simulants. *Adv. Space Res.* 59 (1), 490–495.
- Can, C.A.I., Kai-song, W.U., Xiao-hong, Y., et al., 2015. Damage constitutive model of rock under medium and low strain rates. *Rock Mech. Rock Eng.* 36 (3), 795–802.
- Dong, S., Han, B., Yu, X., et al., 2018. Dynamic impact behaviors and constitutive model of super-fine stainless wire reinforced reactive powder concrete. *Construct. Build. Mater.* 184, 602–616.
- Engelschön, V., Eriksson, S., Cowley, A., et al., 2020. A novel large-volume lunar regolith simulant. *Sci. Rep.* 10 (1), 5473.
- Farries, K.W., Visintin, P., Smith, S.T., et al., 2021. Sintered or melted regolith for lunar construction: state-of-the-art review and future research directions. *Construct. Build. Mater.* 296, 123627.
- Fu, Q., Xie, Y., Long, G., et al., 2017. Impact characterization and modelling of cement and asphalt mortar based on SHPB experiments. *Int. J. Impact Eng.* 106, 44–52.
- Gao, Y.F., Wang, J., Li, Q.Y., et al., 2022. Dynamic response behaviours of Al_2O_3 ceramics with different grain sizes under SHPB compression loading. *Key Eng. Mater.* 922, 45–51.
- GB/T23561.1, 2009. Methods for Determining the Physical and Mechanical Properties of Coal and Rock - Part 1: General Requirements for Sampling. Standardization Administration of China, Beijing, China.
- Ghayoomi, Majid, Suprunenko, Ganna, Mirshekari, Morteza, 2017. Cyclic triaxial test to measure strain-dependent shear modulus of unsaturated sand. *Int. J. Geo-Mech.* 17 (9), 04017043.
- Han, Z., Li, D., Li, X., 2022. Dynamic mechanical properties and wave propagation of composite rock-mortar specimens based on SHPB tests. *Int. J. Min. Sci. Technol.* 32 (4), 793–806.
- Jiang, M., Li, L., Sun, Y., 2012. Properties of TJ-1 lunar soil simulant. *J. Aero. Space. Eng.* 25 (3), 463–469.
- Kanamori, H., Udagawa, S., Yoshida, T., et al., 1998. Properties of lunar soil simulant manufactured in Japan. *Space* 98, 462–468.
- Koohestani, B., Mokhtari, P., Yilmaz, E., et al., 2021. Geopolymerization mechanism of binder-free mine tailings by sodium silicate. *Construct. Build. Mater.* 268, 121217.
- Li, D., Han, Z., Sun, X., et al., 2019. Dynamic mechanical properties and fracturing behavior of marble specimens containing single and double flaws in SHPB tests. *Rock Mech. Rock Eng.* 52, 1623–1643.
- Li, Z., Chen, W., Hao, H., et al., 2021. Dynamic compressive properties of novel lightweight ambient-cured EPS geopolymer composite. *Construct. Build. Mater.* 273, 122044.
- Liu, F., Li, Q.M., 2022. Strain-rate effect of polymers and correction methodology in a SHPB test. *Int. J. Impact Eng.* 161, 104109.
- Liu, J., Liu, B., Wu, Z., et al., 2020. Dynamics and potential applications of a lunar space tethered system. *Acta Astronaut.* 169, 138–149.
- Ma, Q.Y., Gao, C.H., 2018. Effect of basalt fiber on the dynamic mechanical properties of cement-soil in SHPB test. *J. Mater. Civ. Eng.* 30 (8), 04018185.
- Ma, D., Ma, Q., Yao, Z., et al., 2019. Dynamic mechanical properties and failure mode of artificial frozen silty clay subject to one-dimensional coupled static and dynamic loads. *Adv. Civ. Eng.* 2019, 4160804.
- Ma, Q., Ma, D., Yuan, P., et al., 2018. Energy absorption characteristics of frozen soil based on SHPB test. *Adv. Mater. Sci. Eng.* 2018, 5378173.
- Ma, Q.Y., Wang, H.Y., 2022. Analysis of the direct shear test and microstructure of the lunar soil simulant solidified by sodium silicate. *Adv. Mater. Sci. Eng.* 2022, 7654781.
- Momi, J., Lewis, T., Alberini, F., et al., 2021. Study of the rheology of lunar regolith simulant and water slurries for geopolymer applications on the Moon. *Adv. Space Res.* 68 (11), 4496–4504.
- Monkul, M.M., Dacic, A., 2017. Effect of grain size distribution on stress-strain behavior of lunar soil simulants. *Adv. Space Res.* 60 (3), 636–651.
- Montes, C., Broussard, K., Gongre, M., et al., 2015. Evaluation of lunar regolith geopolymer binder as a radioactive shielding material for space exploration applications. *Adv. Space Res.* 56 (6), 1212–1221.
- Ouyang, Z.Y., 2004. Scientific objectives of Chinese lunar exploration project and development strategy. *Adv. Earth Sci.* 19 (3), 351–358.
- Prabu, T., Muthukkumaran, Kasinathan, Venugopal, I., 2022. Assessment of dynamic properties of a new lunar highland soil simulant (LSS-ISAC-1) developed for Chandrayaan missions. *Soil Dynam. Earthq. Eng.* 155, 107178.
- Qian, Y., Xiao, L., Yin, S., et al., 2020. The regolith properties of the Chang'e-5 landing region and the ground drilling experiments using lunar regolith simulants. *Icarus* 337 (2020), 113508.
- Qian, Y., Xiao, L., Wang, Q., et al., 2021. China's Chang'e-5 landing site: geology, stratigraphy, and provenance of materials. *Earth Planet. Sci. Lett.* 561, 116855.
- Ray, C.S., Reis, S.T., Sen, S., et al., 2010. JSC-1A lunar soil simulant: characterization, glass formation, and selected glass properties. *J. Non-Cryst. Solids* 356 (44–49), 2369–2374.
- Ren, G., Wu, H., Fang, Q., et al., 2018. Effects of steel fiber content and type on dynamic compressive mechanical properties of UHPCC. *Construct. Build. Mater.* 164, 29–43.
- Schleppi, J., Gibbons, J., Groetsch, A., et al., 2019. Manufacture of glass and mirrors from lunar regolith simulant. *J. Mater. Sci. Mater. Electron.* 54, 3726–3747.
- Song, X., Hao, Y., Wang, S., et al., 2022b. Dynamic mechanical response and damage evolution of cemented tailings backfill with alkaliized rice straw under SHPB cycle impact load. *Construct. Build. Mater.* 327, 127009.
- Song, L., Hu, S., 2005. Two-wave and three-wave method in SHPB data processing. *Explos. Shock Waves* 4, 368–373.
- Song, Y., Ma, H., Yang, J., et al., 2022a. Dynamic mechanical behaviors and failure mechanism of lignite under SHPB compression test. *Sustainability* 14 (17), 10528.
- Song, L., Xu, J., Fan, S., et al., 2019. Vacuum sintered lunar regolith simulant: pore-forming and thermal conductivity. *Ceram. Int.* 45 (3), 3627–3633.
- Taylor, L.A., Pieters, C.M., Britt, D., 2016. Evaluations of lunar regolith simulants. *Planet. Space Sci.* 126, 1–7.
- Uesugi, K., Tsuchiyama, A., Nakano, T., et al., 2009. 3D shape characterization and image-based DEM simulation of the lunar soil simulant FJS-1. *J. Aero. Space. Eng.* 22, 15–23.
- Wang, Z., Liu, Y., Shen, R.F., 2008. Stress-strain relationship of steel fiber-reinforced concrete under dynamic compression. *Construct. Build. Mater.* 22 (5), 811–819.
- Wang, K.T., Lemougna, P.N., Tang, Q., et al., 2017. Lunar regolith can allow the synthesis of cement materials with near-zero water consumption. *Gondwana Res.* 44, 1–6.
- Xia, K., Rousseau, C.E., Rosakis, A., 2008. Experimental investigations of spontaneous bimaterial interfacial fractures. *J. Mech. Mater. Struct.* 3 (1), 173–184.
- Xiao, S.H., Liao, S.J., Zhong, G.Q., et al., 2021. Dynamic properties of PVA short fiber reinforced low-calcium fly ash-slag geopolymer under an SHPB impact load. *J. Build. Eng.* 44, 103220.
- Xiao, J., Pang, B., Tang, J., et al., 2022. SHPB test of lunar water ice simulant and analysis of reflected wave characteristics. *J. Deep Space Explor.* 9 (2), 150–156.
- Xie, B.J., Yan, Z., 2019. Dynamic mechanical constitutive model of combined coal-rock mass based on overlay model. *J. China Coal Soc.* 44 (2), 463–472.
- Xu, L., Zou, Y., Jia, Y., 2018. China's planning for deep space exploration and lunar exploration before 2030. *Chin. J. Space Sci.* 38, 591–592.
- Xu, D., Zhang, Z., Qin, Y., et al., 2022. Effect of particle size distribution on dynamic properties of cemented coral sand under SHPB impact loading. *Soil Dynam. Earthq. Eng.* 162, 107438.

- Xue, G., Yilmaz, E., Feng, G., et al., 2021. Reinforcement effect of polypropylene fiber on dynamic properties of cemented tailings backfill under SHPB impact loading. *Construct. Build. Mater.* 279, 122417.
- Zarzycki, P.K., Katzer, J., 2019. Multivariate comparison of lunar soil simulants. *J. Aero. Space. Eng.* 32 (5), 06019005.
- Zhang, H., Zhang, X., Zhang, G., et al., 2022. Size, morphology, and composition of lunar samples returned by Chang'E-5 mission, *Science China Physics, Mechanics & Astronomy* 65 (2), 1–8.
- Zheng, Y., Ouyang, Z., Li, C., et al., 2008b. China's lunar exploration program: present and future. *Planet. Space Sci.* 56 (7), 881–886.
- Zheng, D., Song, W., Cao, S., et al., 2021. Investigation on dynamical mechanics, energy dissipation, and microstructural characteristics of cemented tailings backfill under SHPB tests. *Minerals* 11 (5), 542.
- Zhou, S., Yang, Z., Zhang, R., et al., 2021. Preparation and evaluation of geopolymers based on BH-2 lunar regolith simulant under lunar surface temperature and vacuum condition. *Acta Astronaut.* 189, 90–98.
- Zheng, Y.C., Wang, S.J., Ouyang, Z.Y., et al., 2008a. CAS-1 lunar soil simulant. *Adv. Space Res.* 43, 448–454.
- Zhou, R., Cheng, H., Cai, H., et al., 2022. Dynamic characteristics and damage constitutive model of mudstone under impact loading. *Materials* 15 (3), 1128.
- Zou, W., Li, Y., Chen, L., et al., 2016. Mechanical properties of QH-E lunar soil simulant at low confining stresses. *J. Aero. Space. Eng.* 29 (2), 04015036.



Qinyong Ma obtained his BSc and MSc degrees in Mining Engineering from Anhui University of Science and Technology, China, in 1986 and 1993, respectively, and his PhD in Geotechnical Engineering from University of Science and Technology Beijing, China, in 2004. He is a member of the Chinese Society for Rock Mechanics and Engineering. Also, he is the deputy director of the Rock Dynamics Committee of the Chinese Society for Rock Mechanics and Engineering. His research interests include (1) Frozen soil mechanics and engineering; (2) New technology of rapid excavation and support for tunnel and underground engineering; and (3) Concrete structures and new materials. He has been participated in a large number of scientific research projects.